Choice reaction time performance correlates with diffusion anisotropy in white matter pathways supporting visuospatial attention

David S. Tuch*, David H. Salat, Jonathan J. Wisco, Alexandra K. Zaleta, Nathanael D. Hevelone, and H. Diana Rosas

Athinoula A. Martinos Center for Biomedical Imaging, Massachusetts General Hospital, 149 13th Street, Room 2301, Charlestown, MA 02129

Humans exhibit significant interindividual variability in behavioral reaction time (RT) performance yet the underlying neural mechanisms for this variability remain largely unknown. It has been proposed that interindividual variability in RT performance may be due to differences in white matter (WM) physiological properties, although such a relationship has never been demonstrated in cortical projection or association pathways in healthy young adults. Using diffusion tensor MRI (DTI), we sought to test whether diffusion tensor fractional anisotropy (FA), a measure of the orientational coherence of water self-diffusion, is regionally correlated with RT on a visual self-paced choice RT (CRT) task. CRT was found to be significantly correlated with FA in projection and association pathways supporting visuospatial attention including the right optic radiation, right posterior thalamus, and right medial precuneus WM. Significant correlations were also observed in left superior temporal sulcus WM and the left parietal operculum. The lateralization of the CRT–FA correlation to right visual and parietal WM pathways is consistent with the specialization of right visual and parietal cortices for visuospatial attention. The localization of the CRT–FA correlations to predominately visual and parietal WM pathways, but not to motor pathways or the corpus callosum indicates that individual differences in visual CRT performance are associated with variations in the WM underlying the visuospatial attention network as opposed to pathways supporting motor movement or interhemispheric transmission.

diffusion tensor MRI

Behavioral reaction time (RT) performance is widely used in cognitive neuroscience research as a measure of information processing speed. RT performance is known to vary significantly across individuals (1–4), yet little is known about the neural basis for this variability. Identifying the neural substrates for interindividual differences in RT performance would provide invaluable insight into the mechanisms of behavioral performance and information processing speed in health, aging, and psychiatric disorders.

It has been proposed that interindividual differences in RT performance may be due to differences in white matter (WM) physiology, particularly, myelination (1, 5–8). Increased myelination would result in faster (or less variable) nerve conduction velocity (NCV), which would result in faster RTs. The relationship between NCV and WM physiological properties such as myelination and axon diameter is well established (9). However, it is not clear whether interindividual differences in WM physiology are responsible for interindividual differences in RT.

Until recently, it has been difficult to evaluate such a relationship because of the lack of a method for measuring WM microstructural properties *in vivo*. Diffusion tensor imaging (DTI) (10–12) is an MRI technique developed over the last decade that has been shown to provide high sensitivity to WM pathology (13). DTI measures the water self-diffusion tensor within each voxel of the MR image. In cerebral WM, water diffusion is greater in the direction along the axon than in the transverse direction, a phenomenon referred to as diffusion anisotropy.

The physical mechanisms for diffusion anisotropy in WM have not been fully identified, but it is thought that the diffusion barriers presented by the cell membrane and myelin sheath play a significant role (14). Diffusion anisotropy in WM is likely influenced by a number of factors, including the degree of myelination, the density, diameter distribution, and orientational coherence of axons (14), and potentially the diffusion barriers presented by glia. The degree of diffusion anisotropy is conventionally described in terms of the fractional anisotropy (FA) metric (15, 16), which has been referred to as a measure of the "microstructural integrity" of WM tissue (17–19). It is important to emphasize that FA provides only an indirect maker of WM microstructural properties.

DTI has been used to identify WM abnormalities in a wide range of conditions including normal aging (20–22), multiple sclerosis (23), Alzheimer's disease (24, 25), schizophrenia (26, 27), Parkinson's disease (28), epilepsy (29), autism (30), and other disorders. However, there have been only limited reports correlating DTI measures with cognitive or behavioral performance measures in young healthy individuals (17, 31). Klingberg *et al.* (17) reported a correlation between FA and reading ability (Word ID score) in the left temporoparietal junction in both reading-impaired participants ($r = 0.74$) and normal readers ($r = 0.53$). Madden and colleagues (31) reported a moderate correlation ($r = -0.54$) between RT on a visual target detection oddball task and FA in the splenium of the corpus callosum in young healthy adults. This study indicated that FA in WM could be associated with behavioral performance. It remained to be shown that RT and FA are also correlated in specific projection or association pathways. Localization of RT–FA correlations to projection and association pathways is key because a wide number of tasks requiring interhemispheric processing could correlate with FA in callosal WM (32, 33).

The aim of the present study was to determine whether RT performance in young healthy adults and FA are correlated in projection and association WM. DTI was acquired in young healthy participants and the FA metric was regionally correlated with the participants' RT on a self-paced, visual choice RT (CRT) task. CRT and FA were found to be correlated in both projection and association WM pathways, including the right optic radiation, right posterior thalamus, right medial precuneus WM, and left superior temporal WM. Additionally, within-session improvement in CRT performance was found to correlate with FA in the posterior thalamus, right lateral precuneus WM, right superior cuneus WM, and right superior temporal sulcus WM. The localization of the CRT–FA correlation to predominately visual and parietal WM pathways, but not to motor cortical WM or the corpus callosum, indicates that individual differences in CRT performance are associated with variations in the WM underlying the visuospatial
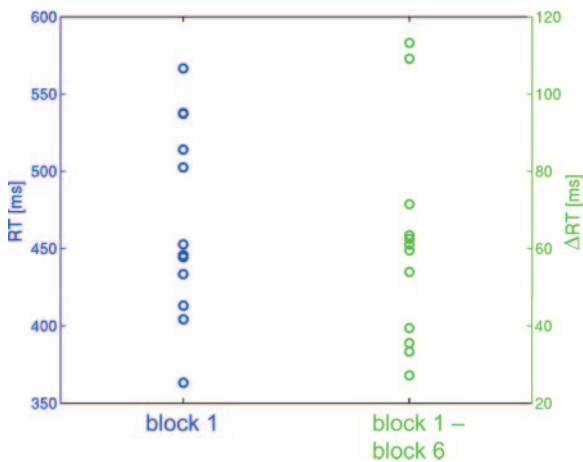
Fig. 1. Behavioral RTs on the CRT task ($n = 12$). The left column gives the participants' RT for native performance (block 1) and the right column gives the ΔRT for within-session improvement (block 1 minus block 6).

attention network as opposed to pathways supporting motor movement or interhemispheric transmission.

Methods

Participants. Twelve young healthy participants (four male, eight female; mean age, 23.2 ± 1.6 years; minimum age, 19.7 years; maximum age, 26.4 years) were studied. All participants were right handed. All participants provided informed written consent by the guidelines of the Massachusetts General Hospital internal review board. The participants gave their informed consent in writing before each of the sessions.

CRT Paradigm. The participants were tested on a self-paced CRT task. The task was the baseline task for a larger study examining implicit motor sequence learning. Four empty squares were presented horizontally on a computer monitor using the E-PRIME software package (Psychology Software Tools, Pittsburgh). The squares were white on a black background. Participants rested the index and middle fingers of both hands on two keys of a four-key response board.

In each trial, one of the four squares (the target square) was filled in solid. The participant responded by pressing the corresponding key on the response board. The targets were presented in a random order with the only exception that no single location was presented twice in a row. The task was repeated in six blocks of 72 trials for a total of 432 trials. Before the session, the participants were instructed to respond as quickly as possible without sacrificing error, and to not correct errors. Between blocks, the participant rested for a 45-s rest period, during which the participant was instructed to make no response. The CRT for block 1 provided an index of native CRT and the ΔCRT between blocks 1 and 6 provided a measure of within-session improvement. The reaction time scores for the participants are given in Fig. 1. No significant correlations were observed between CRT and age ($r_s = 0.34$, P = not significant) or between ΔCRT and age ($r_s = 0.43$, P = not significant).

Image Acquisition. Diffusion tensor MRI scans were obtained on all 12 participants. The scans were performed on a Siemens Sonata 1.5 Tesla MRI scanner (Erlangen, Germany) located at the Athinoula A. Martinos Center for Biomedical Imaging at Massachusetts General Hospital. The DTI acquisition used single-shot EPI (34) and a twice-refocused spin echo sequence (35). The imaging parameters were repetition time (TR) = 9,000 ms, echo time (TE) = 68 ms, $b = 700$ s/mm², $g_{max} = 26$ mT/m, seven directions (one T2 plus six diffusion-weighted), eight averages, total acquisi-

tion time 8 min 33 seconds. The diffusion gradient directions were obtained from the six nonopposed edge-centers of a cube in q space.

Sixty axial oblique slices were acquired. The slices were oriented in the intercommissural (AC–PC) plane. The field of view was 256×256 mm and the matrix size was 128×128 to give 2×2 mm in-plane resolution. The slice thickness was 2 mm (0-mm skip). The mean postaveraged signal-to-noise ratio of the T2 and diffusion-weighted images was 35 and 18, respectively. The eddy current distortions between diffusion weightings were typically less than ≈1–2 voxels.

Preprocessing. Correction for motion and residual eddy current distortion was applied by registering all of the images to the first acquired T2 image. The registration was performed by using FLIRT with a 12-df global affine transformation and a mutual information cost function (36). FLIRT is available through the FSL software library (www.fmrib.ox.ac.uk/fsl). Trilinear interpolation was used for the resampling. The diffusion tensor, associated eigensystem, and FA metric were calculated for each voxel as described (16, 37).

Atlas-Based Analysis. The correlation between CRT and FA was measured by using complementary atlas-based and manual region of interest (ROI) approaches. The atlas-based analysis was performed by normalizing the individual FA volumes to Montreal Neurological Institute (MNI) space by using FLIRT (36). The MNI normalization was performed by registering each individual T2 volume to a skull-stripped version of the MNI 152-subject T2 template (38). The skull-stripping was performed by using the brain BET program (39) from FSL. The transformation from this registration step was then applied to the individual FA volume.

The MNI-normalized FA volumes were smoothed by using a 3D Gaussian kernel with 6-mm full-width at half-maximum (FWHM) and 6-mm spatial extent. The FA volumes were smoothed to increase the statistical sensitivity to correlations equal to or larger than the kernel width. The smoothing width of 6-mm FWHM (= 3 voxel widths) was selected based on numerical evidence that three-voxel FWHM provides sufficient smoothing for 3D Gaussian random fields (40). Voxels with trace diffusion >6 μm^2/ms were not included in the smoothing operation in an effort to minimize the partial volume contribution from cerebrospinal fluid. MNI-normalized FA volumes were also produced by using nearest neighbor interpolation and no smoothing to obtain normalized FA volumes immune from the effects of resampling and smoothing.

The correlation between CRT and FA was computed for each voxel in atlas space. The correlation coefficient was computed by using nonparametric Spearman rank regression (41). Nonparametric Spearman rank regression was used instead of a parametric Pearson regression because of the potential nonnormality of the FA distribution across individuals and the lack of a prior hypothesis that CRT and FA are linearly correlated. The Spearman correlation coefficient (r_s) map was visualized as an overlay on either the MNI single individual T1 template, the group averages FA volume, or a diffusion tensor cuboid map from a representative participant. The representative participant was chosen as the one with the most voxels with the median FA. Voxel-level correlations greater than $r_s > 0.7$ were deemed "high."

Multiple Comparisons Correction. Multiple comparisons correction was applied at the cluster level by using the Monte Carlo permutation method (42). The corrected significance was computed based on the size of voxel clusters at the $P < 0.005$ level. The Monte Carlo calculation used 10^4 trials. Contiguous clusters ≥20 voxels in size (corresponding to a volume of 0.160 cc) were reported. Corrected significance levels of $P < 0.05$ were deemed "significant."

The permutation method was also used to compute the corrected significance thresholds at the voxel level. The corrected voxel-level significance thresholds were reported but were not applied to threshold the data. The voxel-level thresholds were not applied so

Table 1. Cluster analysis of RT–FA correlation

Region	Size, voxels	r_s Median (P value)	r_s Peak (P value)	P_{corr}	MNI coordinates, mm x	y	z
CRT1							
Positive correlations							
Left temporal stem between the superior temporal sulcus and the hippocampal fissure	48	0.84 (1.2×10^{-3})	0.96 (0)	1.6×10^{-2}	−40	−23	−8
Left superior parietal lobule, rostral and superior to the parieto-occipital sulcus	26	0.84 (1.2×10^{-3})	0.97 (0)	NS	−15	−69	64
Right medial precuneus WM	73	0.83 (1.4×10^{-3})	0.96 (0)	6×10^{-3}	11	−64	34
Right posterior thalamus, Meyer's loop, and the anterior segment of the optic radiation	92	0.82 (2.0×10^{-3})	0.94 (0)	3×10^{-3}	22	−27	0
Right optic radiation at the intersection with the posterior forceps of the corpus callosum	41	0.83 (1.7×10^{-3})	0.90 (6.0×10^{-6})	2.4×10^{-2}	30	−60	13
Negative correlations							
Left superior temporal sulcus WM	100	−0.82 (1.7×10^{-3})	−0.94 (0)	2×10^{-3}	−54	−20	−2
Left parietal operculum/inferior posterior insula	31	−0.85 (9.7×10^{-4})	−0.98 (0)	4.8×10^{-2}	−38	−12	−6
Left anterior insula	20	−0.81 (2.4×10^{-3})	−0.89 (9.2×10^{-5})	NS	−32	13	−10
Left superior cerebellum	28	−0.83 (1.7×10^{-3})	−0.93 (0)	NS	−17	−75	−17
Right precentral sulcus WM posterior to the inferior frontal gyrus	21	−0.83 (1.7×10^{-3})	−0.95 (0)	NS	34	9	30
ΔCRT							
Positive correlations							
Left posterior thalamus	39	0.84 (1.2×10^{-3})	0.93 (0)	2.7×10^{-2}	−24	−27	−4
Right lateral precuneus WM	53	0.83 (1.7×10^{-3})	0.92 (0)	1.3×10^{-2}	16	−52	36
Right posterior thalamus	20	0.82 (2.0×10^{-3})	0.94 (0)	NS	24	−29	−2
Right parietio-occipital-temporal WM, at the junction between the arcuate fasciculus and the superior longitudinal fasciculus	24	0.83 (1.4×10^{-3})	0.90 (0)	NS	32	−66	17
Negative correlations							
Left parietal operculum/inferior posterior insula	27	−0.83 (1.4×10^{-3})	−0.88 (1.9×10^{-4})	NS	−36	−10	−2
Right superior cuneus WM	43	−0.84 (1.2×10^{-3})	−0.94 (0)	2.2×10^{-2}	20	−75	30
Right superior temporal sulcus WM	35	−0.80 (3.2×10^{-3})	−0.85 (9.7×10^{-4})	3.5×10^{-2}	42	−35	2

The clusters were defined at the $P < 0.005$ level. Region, anatomic description based on significance cluster. Voxels, spatial extent of cluster in number of voxels; median r_s (P value), median Spearman correlation coefficient in cluster, and associated uncorrected P value, peak r_s (P value); Spearman correlation coefficient for most significant voxel in cluster, and associated uncorrected P value; p_{corr}, significance level for cluster size corrected for multiple comparisons; MNI coordinates, MNI xyz coordinates for most significant voxel in cluster. NS, not significant at the corrected $P < 0.05$ level. P values of identically zero are due to the tail behavior of the Spearman model. The clusters are extended in space, and so the MNI location of the peak correlation may not be representative of the entire cluster location. Only contiguous clusters ≥20 voxels in size (corresponding to a volume of 0.160 cc) are reported.

that the anatomic continuity of the correlation maps could be visualized.

ROI Analysis. Confirmatory ROIs were defined in each individual participant's MNI-normalized T2 volume. The FA volumes were MNI-normalized to account for differences in head orientation and to provide optimal matching of regions across individuals. The FA values were sampled from FA volumes that had been MNI-normalized by using nearest neighbor resampling and had not been smoothed, thus eliminating the smoothing effects of resampling and kernel smoothing.

ROIs were placed in a total of 10 areas. The areas were selected based on significant clusters identified in the atlas-based analysis, or to serve as control regions. The 10 anatomic areas included the optic radiations of each hemisphere, the genu and splenium of the corpus callosum, the anterior and posterior thalamus in each hemisphere, and the posterior limb of the internal capsule in each hemisphere. All ROIs were created from small swaths within the WM to attempt to reduce partial volume contamination. The posterior limb of the internal capsule was included as an ROI to test for an effect in motor WM.

The ROIs were defined as follows. The optic radiation was defined in the axial view on a slice approximating the center of the splenium of the corpus callosum and the ventricles displaying the most lateral extent, and drawn lateral to the lateral ventricle, spanning the most posterior aspect of the ventricle, from the region where the posterior callosal fibers intersect with the optic radiations to the most lateral aspect of the posterior ventricular region. The

genu and the splenium of the corpus callosum were drawn in the axial view, defined as a line of voxels spanning a portion of the medial/lateral extent of the approximate center of each region of the callosum. Thalamic ROIs were created as a 3D crosshairs (seven voxels) to attempt to sample from a homogeneous region within the structure, and were drawn on an axial slice approximating the center of the thalamus placed in the anterior- and posterior-most regions while staying completely within the structure. The posterior limb of the internal capsule was drawn as a line of voxels down the

Table 2. Correlation coefficients from ROI analysis

ROI	r_s (P value) CRT1	r_s (P value) ΔCRT	Size ± SD, voxels
R optic radiation	0.83 (1.7×10^{-3})	0.69 (1.6×10^{-2})	24.5 ± 4.08
L optic radiation	0.31 (NS)	0.36 (NS)	23.4 ± 3.17
R ant thalamus	0.30 (NS)	0.24 (NS)	7 ± 0
L ant thalamus	−0.09 (NS)	0 (NS)	7 ± 0
R post thalamus	0.55 (NS)	0.66 (2.4×10^{-2})	7 ± 0
L post thalamus	0.55 (NS)	0.71 (1.3×10^{-2})	7 ± 0
Genu	−0.02 (NS)	0.10 (NS)	17 ± 1.59
Splenium	−0.19 (NS)	−0.22 (NS)	24.1 ± 1.56
R post int capsule	0.50 (NS)	0.24 (NS)	15.3 ± 1.91
L post int capsule	0.15 (NS)	0.15 (NS)	15.3 ± 1.88

The Spearman correlation coefficient r_s (and associated two-sided P value) is listed for the correlation between FA and native CRT (CRT1) and between FA and within-session improvement in CRT (ΔCRT). NS, not significant at the $P < 0.05$ level. ant, anterior; post, posterior; int, internal; R, right; L, left.
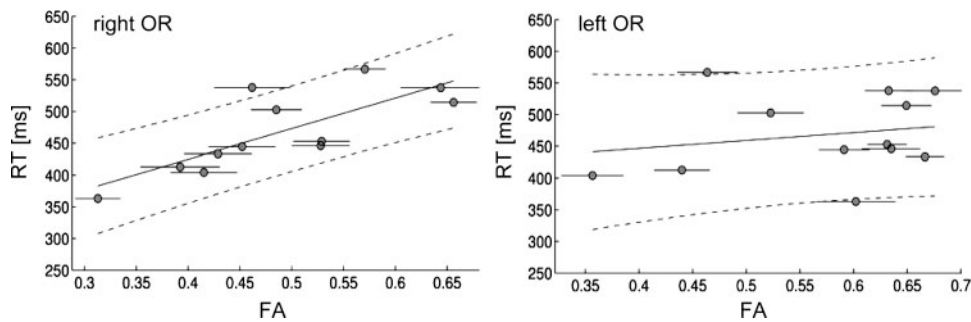
Fig. 2. CRT performance is correlated with FA in the right optic radiation but not the left optic radiation. The plots show the native CRT and the ROI FA measurements (±SEM) from the right and left optic radiation. CRT and FA are significantly correlated in the right optic radiation ($r_s = 0.83$, $P = 1.7 \times 10^{-3}$) but not the left optic radiation ($r_s = 0.31$, P = not significant) (Table 2). The solid line indicates the linear fit, and the dashed line indicates the 85% confidence interval for the fit.

center of the structure in the axial view on a slice approximating the center of the genu of the corpus callosum, where the inflection between the anterior limb and posterior limb was greatest.

Results

The participants' native CRT (block 1) and within-session improvement in CRT (block 1 minus block 6) are shown in Fig. 1. Table 1 provides a list of all anatomic regions where significant (corrected $P < 0.05$) correlations between CRT and FA were observed. Significant clusters of positive correlation between native CRT and FA were found in the right posterior thalamus, right optic radiation, right medial precuneus WM, and left superior temporal sulcus WM. Negative correlations were found in left superior temporal sulcus WM and the left parietal operculum. The positive correlations for within-session improvement in CRT localized to the left posterior thalamus and right precuneus WM, and the negative correlations localized to right superior cuneus WM and right superior temporal sulcus WM.

The ROI analysis showed that native CRT was significantly correlated with FA in the right optic radiation but not the left (Table 2 and Fig. 2). Within-session improvement in CRT was significantly correlated with FA in the right optic radiation and both hemispheres of the posterior thalamus (Table 2). No significant correlations were observed for the corpus callosum ROIs or the poster limb of the internal capsule.

The individual FA maps showed a clear increase in FA in the right optic radiation with increasing CRT (Fig. 3). The correlation between CRT and FA localized to the right visual pathway (Fig. 4), extending from the lateral geniculate nucleus through Meyer's loop to the optic radiation, terminating at the junction between the optic radiation and the posterior forceps of the corpus callosum. The correlation maps for within-session improvement in CRT are shown in Fig. 5A. The diffusion tensor maps in Fig. 5B show that the ΔCRT–FA correlation lies in the posterior thalamus at the border between the pulvinar and lateral geniculate nucleus.

Discussion

DTI in young healthy adults revealed significant correlations between CRT and FA in right thalamus, and right visual, right medial precuneus, and left superior temporal WM. The ROI analysis for within-session improvement in CRT indicated correlations in both hemispheres of the posterior thalamus in the region of the lateral geniculate and pulvinar nuclei.

The right visual and right parietal cortices are specialized for visuospatial attention (43–46). The pulvinar nucleus, located in the posterior thalamus, is a key node in the visuospatial attention network (47). Superior temporal gyrus has been implicated in visual awareness (48) and voluntary control of visuospatial attention (49). No significant correlations were observed in the posterior limb of the internal capsule or the corpus callosum for either experiment.
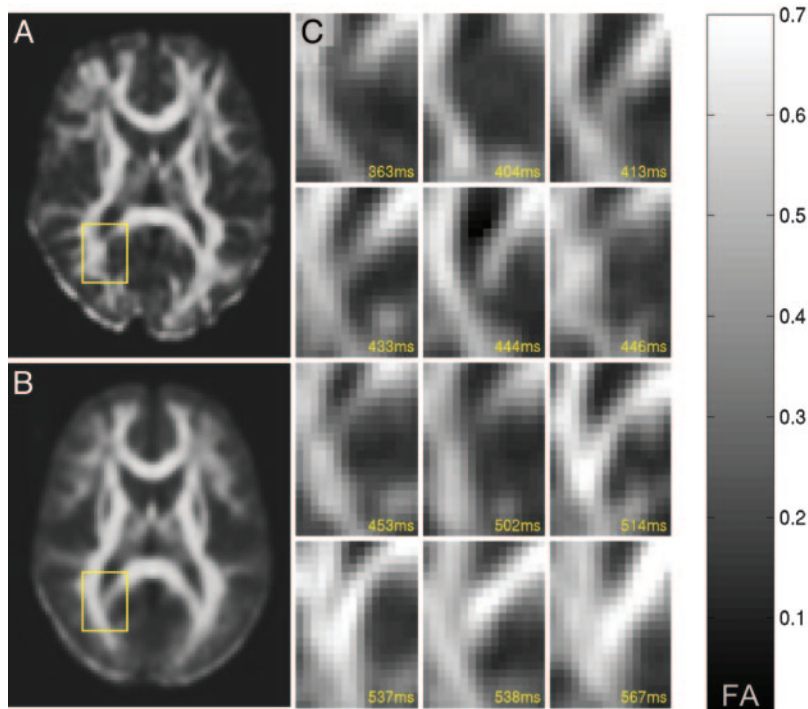
Fig. 3. Individuals with fast CRT have low FA in the right optic radiation. MNI-normalized FA maps for the representative participant (A) and the group average FA map (B) are shown. The yellow box indicates a region of interest (ROI) at the junction between the right optic radiation and the posterior forceps of the corpus callosum. (C) FA maps from each of the 12 participants taken from the ROI. Each participant's CRT for block 1 is shown at the bottom right corner of that participant's map. The ROIs are ordered from left to right and top to bottom in order of increasing RT. Note the increase in FA in the optic radiation with increasing CRT. The images are displayed in radiological convention so that the left direction on the page corresponds to the right direction on the anatomy and vice versa. The radiological display convention is used throughout.
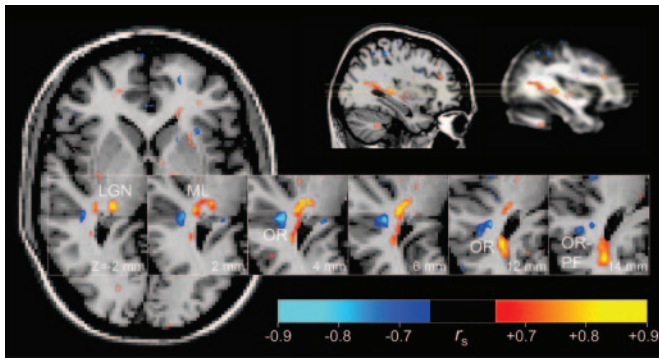
Fig. 4. CRT and FA are correlated in the right visual pathway. The Spearman correlation coefficient (r_s) between CRT and FA is displayed as a colored map overlaid on the MNI individual T1 template. The small frames show six axial slices through the optic radiation. The superior–inferior level of the axial slices is indicated by the yellow lines in the sagittal images at top right and by the MNI Z-coordinate at the bottom right of each frame. The sagittal images at top right are the MNI individual T1 template (*Left*) and the group average FA map (*Right*). The correlation map shows the trajectory of the right visual pathway from lateral geniculate nucleus (LGN) through Meyer's loop (ML) to the optic radiation (OR), terminating at the junction between the optic radiation and the posterior forceps of the corpus callosum (OR-PF). Multiple comparisons-corrected significance levels of $P < 0.05$ and $P < 0.10$ are achieved by critical correlation values of $|r_s| > 0.867$ and $|r_s| > 0.839$, respectively.

These results indicate that native performance and within-session improvement in CRT are associated with variations in the WM, supporting visuospatial attention as opposed to pathways supporting motor movement or interhemispheric transmission.

Madden and colleagues (31) reported a correlation between RT on a visual oddball task and FA in the splenium of the corpus callosum. The present study found that RT-FA correlations are also present in the thalamus and projection and association pathways, are lateralized, and also hold for within-session improvement in RT. No significant correlations were found in the splenium of the corpus callosum, which could be due to differences in the behavioral paradigm or experimental protocol for this study and ref. 31.

The physiological mechanisms for the observed CRT–FA correlation require substantial further investigation. FA is influenced by a number of factors including, but not limited to, myelination, axon diameter, axon density, and ultrastructure (14). The correlation may be due to the influence of myelin thickness on both water self-diffusion (14) and NCV (9). The myelin hypothesis would predict a negative correlation between CRT and FA because increased myelin thickness would cause increased FA and faster NCV, which would in turn result in faster RT. However, the CRT–FA correlations were predominantly positive, particularly in the right optic radiation and the posterior thalamus (Tables 1 and 2).

The positivity of the CRT–FA correlation may be due to the effect being mediated by factors other than myelin. Significant RT-FA correlations were observed in the thalamus despite its low myelin content compared to WM (50). In both WM and thalamus, physiological factors other than myelin that could influence the correlation include intravoxel fiber crossing or axon diameter. In anatomic regions containing intravoxel fiber crossing (51), increased FA of an individual fiber population can result in a decrease in the overall FA (52, 53). For example, in the junction between the optic radiation and the posterior forceps (Figs. 3 and 4) a selective increase in the FA of the optic radiation could result in a decrease in the overall FA. The fiber crossing effect might also be a factor in Meyer's loop where the rapidly bending fibers produce intravoxel orientational dispersion (54). The relationship between composite fiber architecture and FA can be clarified with diffusion MRI
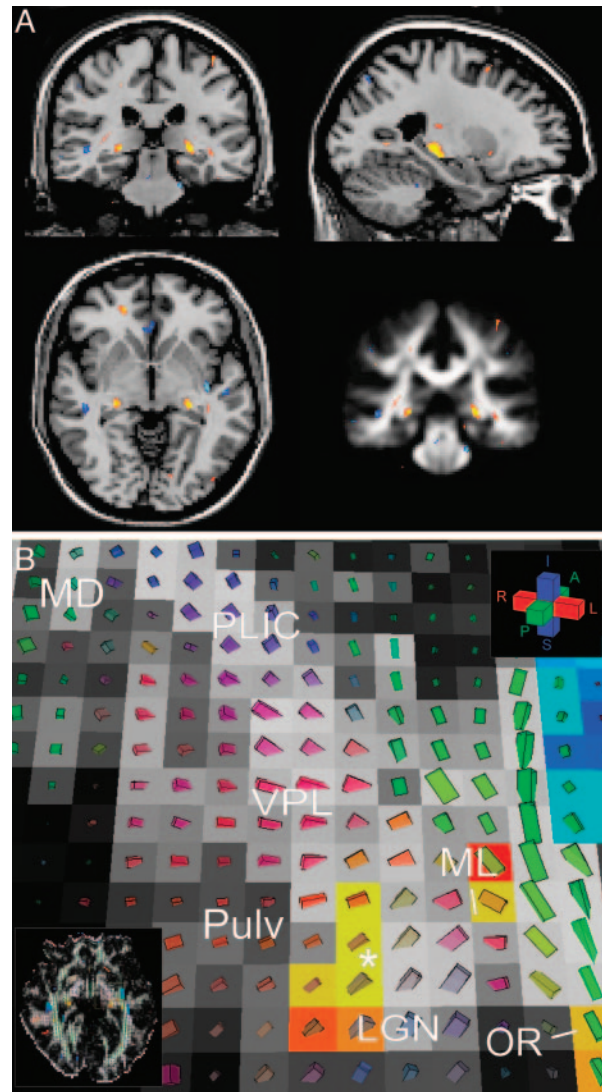

Fig. 5. Within-session improvement in CRT is correlated with FA in the posterior thalamus. (*A*) The Spearman correlation coefficient map for ΔCRT–FA is shown superimposed on the MNI individual T1 template (*Upper* and *Lower Left*), and on a coronal view of the group average FA map (*Lower Right*). The color scale for the correlation coefficient map is the same as described in Fig. 4. The correlation localizes to left and right posterior thalamus. (*B*) Diffusion tensor map of the left thalamus from the representative participant. The group ΔCRT–FA correlation coefficient map is shown superimposed as a red–yellow color scale image on a diffusion tensor cuboid map. The color scale for the correlation map is the same as described in Fig. 4. The region of significant correlation (indicated by the asterisk) localizes to the border between the pulvinar nucleus (red, medial–lateral) and the lateral geniculate nucleus (blue-red, posterior–medial to inferior–lateral). The cuboidal glyphs depict the 3D diffusion tensor at each voxel location. The axes of each cuboid are oriented and scaled according to the local diffusion tensor eigensystem. An additional scaling factor of sqrt(FA) is also applied. The cuboids are colored according the orientation of the principal eigenvector with red indicating medial–lateral, green anterior–posterior, and blue superior–inferior (59). The directional color scheme is also indicated by the red–green–blue crossbars in the upper right corner. LGN, lateral geniculate nucleus; MD, mediodorsal nucleus; ML, Meyer's loop; PLIC, posterior limb of the internal capsule; Pulv, pulvinar nucleus; VPL, ventral posterior lateral nucleus (60). Note that the slice is shown at an oblique angle.

methods which can resolve intravoxel structure such as q-space imaging (55) and high angular resolution diffusion imaging (51, 54).

The CRT–FA correlations may also be caused by interindividual differences in axon diameter distribution. Large caliber axons, e.g., magnocellular axons, have faster NCVs, which could result in faster

CRT. The relationship between axon diameter and FA is not fully known, although increased axon diameter could result in lower FA due to an increase in the mobility of water in the intraaxonal compartment (56).

The positive correlation may also be due to interference effects, although this mechanism is regarded as unlikely. Faster NCV in the optic radiation could result in slower CRT because of interference between the early visual processing components and the subsequent target identification and motor response programming components of the CRT task. This hypothesis could be tested by measuring the correlation between FA and simple RT or the latency for the P100 visual evoked response.

The correlations reported here may potentially reflect an associative as opposed to a causal relationship. It will be necessary to investigate the influence of other physiological factors such as the length of the optic radiation and the surface area and thickness of primary visual cortex. Detecting changes in FA with learning or skill acquisition would also address the issue of causality.

The correlation between CRT and FA was assessed by using both an atlas-based analysis and an ROI approach. The atlas-based analysis and the ROI analysis provided complementary information. For example, for the ΔCRT experiment, the right posterior thalamus failed to achieve significance at the cluster level (Table 1), but the correlation was significant in the ROI analysis (Table 2).

The present study examined the correlation between FA and behavioral RT performance. It will also be possible to extend this method to examine the correlation between FA and more direct measures of information processing speed obtained with electroencephalography (EEG) or magnetoencephalography (MEG). For example, correlating FA with event-related potential latency or phase offset for synchronous brain activity measured on EEG or MEG could identify WM pathways that mediate interindividual differences in information processing speed for specific cognitive tasks.

It remains to be determined to what extent the CRT–FA is caused by genetic or epigenetic factors. Pfefferbaum *et al.* (57) found that FA in the corpus callosum in old age is genetically regulated, with the FA of the splenium of the corpus callosum being more strongly regulated than that of the genu. RTs have been found to be moderately to highly heritable (58). In light of the correlation between CRT and FA, the heritability of both CRT and FA points to the question of whether the two measures share common genetic factors. It should be possible to address this question by examining the correlation between CRT and FA in a twin design. Identifying the genetic and epigenetic contributions to CRT–FA correlation will help shed light on the fundamental role of WM physiology in human cognitive performance.

1. Luciano, M., Wright, M. J., Geffen, G. M., Geffen, L. B., Smith, G. A. & Martin, N. G. (2004) *Behav. Genet.* **34,** 41–50.
2. Vernon, P. A. (1989) *Pers. Individ. Dif.* **10,** 573–576.
3. Ho, H. Z., Baker, L. A. & Decker, S. N. (1988) *Behav. Genet.* **18,** 247–261.
4. Vernon, P. A. (1987) *Speed of Information-Processing and Intelligence* (Ablex, Norwood, CT).
5. Reed, T. E., Vernon, P. A. & Johnson, A. M. (2004) *Neuropsychologia* **42,** 1709–1714.
6. Posthuma, D., Baare, W. F., Hulshoff Pol, H. E., Kahn, R. S., Boomsma, D. I. & De Geus, E. J. (2003) *Twin Res.* **6,** 131–139.
7. Posthuma, D., de Geus, E. J. C. & Boomsma, D. I. (2001) *Behav. Genet.* **31,** 593–602.
8. Miller, E. M. (1994) *Pers. Individ. Dif.* **17,** 803–832.
9. Jack, J. J. B., Noble, D. & Tsien, R. W. (1983) *Electrical Current Flow in Excitable Cells* (Oxford Univ. Press, Oxford).
10. Basser, P. J., Mattiello, J. & LeBihan, D. (1994) *Biophys. J.* **66,** 259–267.
11. Pierpaoli, C., Jezzard, P., Basser, P. J., Barnett, A. & Di Chiro, G. (1996) *Radiology* **201,** 637–648.
12. Le Bihan, D. (2003) *Nat. Rev. Neurosci.* **4,** 469–480.
13. Dong, Q., Welsh, R. C., Chenevert, T. L., Carlos, R. C., Maly-Sundgren, P., Gomez-Hassan, D. M. & Mukherji, S. K. (2004) *J. Magn. Reson. Imaging* **19,** 6–18.
14. Beaulieu, C. (2002) *NMR Biomed.* **15,** 438–455.
15. Basser, P. J. (1997) *Ann. N.Y. Acad. Sci.* **820,** 123–138.
16. Pierpaoli, C. & Basser, P. J. (1996) *Magn. Reson. Med.* **36,** 893–906.
17. Klingberg, T., Hedehus, M., Temple, E., Salz, T., Gabrieli, J. D., Moseley, M. E. & Poldrack, R. A. (2000) *Neuron* **25,** 493–500.
18. Head, D., Buckner, R. L., Shimony, J. S., Williams, L. E., Akbudak, E., Conturo, T. E., McAvoy, M., Morris, J. C. & Snyder, A. Z. (2004) *Cereb. Cortex* **14,** 410–423.
19. Pfefferbaum, A., Rosenbloom, M. & Sullivan, E. V. (2002) *Alcohol Clin. Exp. Res.* **26,** 1031–1046.
20. Salat, D. H., Tuch, D. S., Greve, D. N., van der Kouwe, A. J., Hevelone, N. D., Zaleta, A. K., Rosen, B. R., Fischl, B., Corkin, S., Rosas, H. D. & Dale, A. M. (2005) *Neurobiol. Aging* **26,** 1215–1227.
21. Pfefferbaum, A., Sullivan, E. V., Hedehus, M., Lim, K. O., Adalsteinsson, E. & Moseley, M. (2000) *Magn. Reson. Med.* **44,** 259–268.
22. Moseley, M. (2002) *NMR Biomed.* **15,** 553–560.
23. Filippi, M., Cercignani, M., Inglese, M., Horsfield, M. A. & Comi, G. (2001) *Neurology* **56,** 304–311.
24. Bozzali, M., Falini, A., Franceschi, M., Cercignani, M., Zuffi, M., Scotti, G., Comi, G. & Filippi, M. (2002) *J. Neurol. Neurosurg. Psychiatry* **72,** 742–746.
25. Rose, S. E., Chen, F., Chalk, J. B., Zelaya, F. O., Strugnell, W. E., Benson, M., Semple, J. & Doddrell, D. M. (2000) *J. Neurol. Neurosurg. Psychiatry* **69,** 528–530.
26. Kubicki, M., Westin, C. F., Nestor, P. G., Wible, C. G., Frumin, M., Maier, S. E., Kikinis, R., Jolesz, F. A., McCarley, R. W. & Shenton, M. E. (2003) *Biol. Psychiatry* **54,** 1171–1180.
27. Lim, K. O., Hedehus, M., Moseley, M., de Crespigny, A., Sullivan, E. V. & Pfefferbaum, A. (1999) *Arch Gen. Psychiatry* **56,** 367–374.
28. Yoshikawa, K., Nakata, Y., Yamada, K. & Nakagawa, M. (2004) *J. Neurol. Neurosurg. Psychiatry* **75,** 481–484.
29. Eriksson, S. H., Rugg-Gunn, F. J., Symms, M. R., Barker, G. J. & Duncan, J. S. (2001) *Brain* **124,** 617–626.
30. Barnea-Goraly, N., Kwon, H., Menon, V., Eliez, S., Lotspeich, L. & Reiss, A. L. (2004) *Biol. Psychiatry* **55,** 323–326.
31. Madden, D. J., Whiting, W. L., Huettel, S. A., White, L. E., MacFall, J. R. & Provenzale, J. M. (2004) *Neuroimage* **21,** 1174–1181.
32. Jerger, J., Martin, J. & McColl, R. (2004) *J. Am. Acad. Audiol.* **15,** 79–87.
33. Schulte, T., Sullivan, E. V., Muller-Oehring, E. M., Adalsteinsson, E. & Pfefferbaum, A. (2005) *Cereb. Cortex*, in press.
34. Liu, G., van Gelderen, P., Duyn, J. & Moonen, C. T. (1996) *Magn. Reson. Med.* **35,** 671–677.
35. Reese, T. G., Heid, O., Weisskoff, R. M. & Wedeen, V. J. (2003) *Magn. Reson. Med.* **49,** 177–182.
36. Jenkinson, M., Bannister, P., Brady, M. & Smith, S. (2002) *Neuroimage* **17,** 825–841.
37. Basser, P. J., Mattiello, J. & LeBihan, D. (1994) *J. Magn. Reson. B.* **103,** 247–254.
38. Mazziotta, J. C., Toga, A. W., Evans, A., Fox, P. & Lancaster, J. (1995) *Neuroimage* **2,** 89–101.
39. Smith, S. M. (2002) *Hum. Brain Mapp.* **17,** 143–155.
40. Nichols, T. & Hayasaka, S. (2003) *Stat. Methods Med. Res.* **12,** 419–446.
41. Hollander, M. & Wolfe, D. A. (1999) *Nonparametric Statistical Methods* (Wiley, New York).
42. Nichols, T. E. & Holmes, A. P. (2002) *Hum. Brain Mapp.* **15,** 1–25.
43. Nobre, A. C., Sebestyen, G. N., Gitelman, D. R., Mesulam, M. M., Frackowiak, R. S. & Frith, C. D. (1997) *Brain* **120,** 515–533.
44. Corbetta, M., Miezin, F. M., Shulman, G. L. & Petersen, S. E. (1993) *J. Neurosci.* **13,** 1202–1226.
45. Weintraub, S. & Mesulam, M. M. (1987) *Arch Neurol.* **44,** 621–625.
46. Mesulam, M. M. (1981) *Ann. Neurol.* **10,** 309–325.
47. Petersen, S. E., Robinson, D. L. & Morris, J. D. (1987) *Neuropsychologia* **25,** 97–105.
48. Karnath, H. O., Ferber, S. & Himmelbach, M. (2001) *Nature* **411,** 950–953.
49. Hopfinger, J. B., Buonocore, M. H. & Mangun, G. R. (2000) *Nat. Neurosci.* **3,** 284–291.
50. Smith, M. E. (1973) *J. Lipid Res.* **14,** 541–551.
51. Tuch, D. S., Reese, T. G., Wiegell, M. R. & Wedeen, V. J. (2003) *Neuron* **40,** 885–895.
52. Pierpaoli, C., Barnett, A., Pajevic, S., Chen, R., Penix, L. R., Virta, A. & Basser, P. (2001) *Neuroimage* **13,** 1174–1185.
53. Wiegell, M. R., Larsson, H. B. & Wedeen, V. J. (2000) *Radiology* **217,** 897–903.
54. Tuch, D. S. (2004) *Magn. Reson. Med.* **52,** 1358–1372.
55. Callaghan, P. T. (1993) *Principles of Nuclear Magnetic Resonance Microscopy* (Oxford Univ. Press, Oxford).
56. Takahashi, M., Hackney, D. B., Zhang, G., Wehrli, S. L., Wright, A. C., O'Brien, W. T., Uematsu, H., Wehrli, F. W. & Selzer, M. E. (2002) *Proc. Natl. Acad. Sci. USA* **99,** 16192–16196.
57. Pfefferbaum, A., Sullivan, E. V. & Carmelli, D. (2001) *NeuroReport* **12,** 1677–1681.
58. Posthuma, D., Mulder, E. J., Boomsma, D. I. & de Geus, E. J. (2002) *Biol. Psychol.* **61,** 157–182.
59. Pajevic, S. & Pierpaoli, C. (1999) *Magn. Reson. Med.* **42,** 526–540.
60. Wiegell, M. R., Tuch, D. S., Larsson, H. B. & Wedeen, V. J. (2003) *Neuroimage* **19,** 391–401.

NEUROSCIENCE